A dielectric-defined lateral heterojunction in a monolayer semiconductor

M. Iqbal Bakti Utama[1,2,3,8], Hans Kleemann[1,4,8], Wenyu Zhao[1], Chin Shen Ong[1,3], Felipe H. da Jornada [1,3], Diana Y. Qiu[1,3], Hui Cai[5], Han Li[5], Rai Kou [1], Sihan Zhao[1], Sheng Wang [1,3], Kenji Watanabe [6], Takashi Taniguchi[6], Sefaattin Tongay[5], Alex Zettl[1,3,7], Steven G. Louie [1,3] and Feng Wang [1,3,7]*

Owing to their low dimensionality, two-dimensional semiconductors, such as monolayer molybdenum disulfide, have a range of properties that make them valuable in the development of nanoelectronics. For example, the electronic bandgap of these semiconductors is not an intrinsic physical parameter and can be engineered by manipulating the dielectric environment around the monolayer. Here we show that this dielectric-dependent electronic bandgap can be used to engineer a lateral heterojunction within a homogeneous MoS$_2$ monolayer. We visualize the heterostructure with Kelvin probe force microscopy and examine its influence on electrical transport experimentally and theoretically. We observe a lateral heterojunction with an approximately 90 meV band offset due to the differing degrees of bandgap renormalization of monolayer MoS$_2$ when it is placed on a substrate in which one segment is made from an amorphous fluoropolymer (Cytop) and another segment is made of hexagonal boron nitride. This heterostructure leads to a diode-like electrical transport with a strong asymmetric behaviour.

Atomically thin semiconductors, such as monolayer transition metal dichalcogenides (TMDs)[1–3], provide a platform for investigating nanoscale quantum phenomena[4–6] and have a range of potential applications in nanoelectronics[7–9]. A freestanding monolayer of a TMD experiences a reduced dielectric screening and an enhanced Coulomb interaction by virtue of its atomically thin structure. In contrast to bulk materials, electric field lines between charges inside a monolayer can extend substantially outside of the layer[10–12]. This leads to an ineffective intrinsic screening that enhances electronic interactions and leads to large exciton binding energies between 0.2 and 0.7 eV in these materials[10–18]. Furthermore, the electronic band structure of atomically thin two-dimensional (2D) layers is not completely intrinsic to the material and can be strongly affected by the surrounding environment[13,19–23]. With both electron and hole experiencing the screening, the conduction and valence band edges shift in opposite directions[12,13,21,23]. Ab initio calculations predict that there is a monotonic decrease of electronic bandgap energy with increasing dielectric screening, where the reduction of the bandgap can reach the order of hundreds of millielectronvolts relative to the bandgap of a freestanding monolayer[13,20,22,24–27]. Recent scanning tunnelling spectroscopy[13] and optical spectroscopy[20,22] studies provided evidence that the bandgap renormalization phenomenon in atomically thin 2D semiconductors can indeed be substantial. Such bandgap renormalization may have a profound effect on electrical transport in atomically thin 2D semiconductors. However, the effect has not been investigated thoroughly and its implications in the development of applications based on 2D materials remains unclear.

In this Article, we report the design of lateral heterojunctions within a homogeneous MoS$_2$ monolayer, exploiting the dielectric-dependent bandgap renormalization, and explore its influence on electrical transport. We prepared a continuous monolayer MoS$_2$ which has a segment on a substrate with a high dielectric constant (ε) and an adjacent segment on a substrate with a low ε (Fig. 1a). Owing to the different degrees of renormalization of the electronic bandgap introduced by the two substrates on each segment, the monolayer MoS$_2$ forms an in-plane type-I heterojunction above the boundary of the two substrates (Fig. 1b, c). We used this sample configuration to perform Kelvin probe force microscopy (KPFM) and electrical transport measurements across the heterojunction. KPFM[28,29] examines the local variation of surface potential across the device channel[30] and provides a direct determination of the band offset of the MoS$_2$ heterojunction from the dielectric engineering. Electrical measurements show that the presence of the heterostructure has a significant effect on electrical transport through the device, leading to a strong asymmetric rectification behaviour. The experimentally observed transport phenomena can also be qualitatively reproduced in a numerical simulation of the device, which exhibits several unique aspects arising from the atomically thin layers. Such dielectric-defined heterostructure behaviour can be important for understanding electrical transport behaviour in atomically thin 2D layers and provides a new approach for engineering 2D nanoelectronic devices[4,31].

Theoretical calculations[21,23,32,33] show that the change in the bandgap of the 2D layer due to the dielectric screening effect by the substrate(s) is most dramatic when the 2D layer has a low intrinsic ε. In addition, a high contrast from the dielectric screening environment involving a substrate with low ε_{low} and a substrate with high ε_{high} is desirable to introduce a significant change in the bandgap of the 2D layer at the heterojunction. We choose the fluoropolymer

[1]Department of Physics, University of California at Berkeley, Berkeley, CA, USA. [2]Department of Materials Science and Engineering, University of California at Berkeley, Berkeley, CA, USA. [3]Materials Science Division, Lawrence Berkeley National Laboratory, Berkeley, CA, USA. [4]Institut für Angewandte Photophysik, Technische Universität Dresden, Dresden, Germany. [5]School for Engineering of Matter, Transport and Energy, Arizona State University, Tempe, AZ, USA. [6]National Institute for Materials Science, Tsukuba, Japan. [7]Kavli Energy NanoSciences Institute at University of California Berkeley and Lawrence Berkeley National Laboratory, Berkeley, CA, USA. [8]These authors contributed equally: M. Iqbal Bakti Utama, Hans Kleemann. *e-mail: fengwang76@berkeley.edu
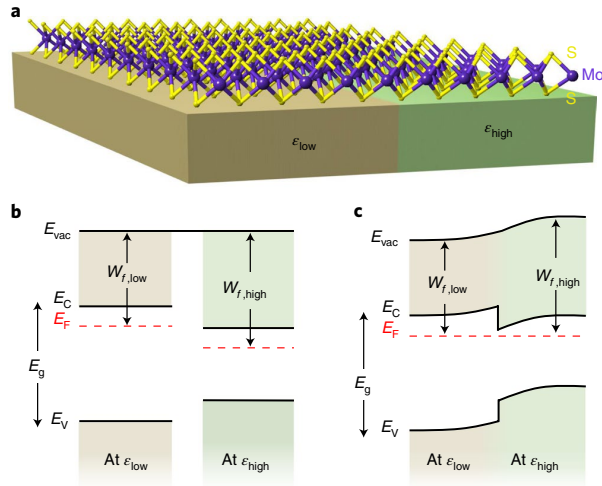
Fig. 1 | Engineering 2D heterojunctions through dielectric-dependent bandgap renormalization. a, Schematic illustration of the heterostructure. Two substrates with different dielectric constant ($\varepsilon_{\text{low}} < \varepsilon_{\text{high}}$) are used to locally vary the MoS$_2$ electronic bandgap. **b**, The expected band alignment of isolated monolayer MoS$_2$ situated on the low-ε substrate (Cytop) and on the high-ε substrate (hBN), respectively. The segments of MoS$_2$ monolayers on Cytop and on hBN are assumed to have the same electron doping density from the electrostatic gating. **c**, The band alignment from **b** if the MoS$_2$ segments on the two substrates are in contact and reach equilibrium following Anderson's rule. A type-I lateral heterojunction forms with an energy barrier for electron transport in the conduction band.

Cytop ($\varepsilon = 2.0–2.1$) and hBN ($\varepsilon(0) = 6.9$, $\varepsilon(\infty) = 5.0$ normal to c-axis[34]) to serve as the low-ε and high-ε substrates, respectively. The fluoropolymer Cytop substrate is one of the materials with the lowest dielectric constant that still allows ease of processing and device fabrication. Meanwhile, the straight edges of as-exfoliated thin hBN flakes provide a boundary that is atomically sharp for a well defined junction area. Moreover, both Cytop[35] and hBN[36] are known to be insulating layers with a low density of surface trap states.

Heterojunction device design and electrical measurement

We transferred a monolayer of MoS$_2$ atop the boundary of a hBN flake on a Cytop film and then fabricated electrical contacts onto the monolayer to form a device channel that is perpendicular to the Cytop/hBN substrate boundary (Fig. 2a). The electrical measurements are then performed in a four-terminal configuration to minimize the influence of contacts. Figure 2b shows the current–voltage (I–V) measurement of the device for different back gate–source voltages (which we shall refer to as 'gate voltage' for brevity) $V_{\text{gs}} > 0\,\text{V}$, which correspond to electron doping. With the MoS$_2$ segment on Cytop grounded, the device exhibited a rectification behaviour that is reminiscent of a diode. This rectification behaviour is consistent with the expected type-I heterojunction formation drawn in Fig. 1c, where the MoS$_2$ segments above the low-ε and high-ε substrates have different electronic bandgaps due to dielectric screening. This behaviour is similar to a n–n heterojunction with the MoS$_2$ segment on Cytop (hBN) containing the depletion (accumulation) regime[37].

In comparison, the reference MoS$_2$ monolayer device on a uniform Cytop film exhibits linear Ohmic-like behaviour (Fig. 2c), suggesting that the rectification arises from the presence of the heterojunction at the boundary between the high-ε and low-ε substrates. Furthermore, we also conducted control experiments with a MoS$_2$ monolayer on a step edge of a hBN flake that otherwise

supports a uniform dielectric environment (Supplementary Fig. 7). Such a control device shows symmetric output curves, which also substantiates that the rectification cannot be attributed only to the presence of the step edge (for example, strain-induced or otherwise) without introducing dielectric contrast.

A prominent feature of our MoS$_2$ heterojunction device behaviour is that the I–V curve at forward bias (that is, higher than $V_{\text{ch}} \approx 0.1\,\text{V}$) is mostly linear. This behaviour is commonly found in real diodes, which can be described by a piecewise linear model with a 'turn-on' voltage (V_{t}) before the device appears to be Ohmic-like[38]. The turn-on voltage is often correlated with the potential landscape of the diode (for example, the built-in voltage in Si p–n diodes), and it provides an estimate of the conduction band offset across the heterojunction. Our low-temperature transport measurements yield a turn-on voltage $V_{\text{t}} \sim 90\,\text{mV}$ in the device (17 K, Fig. 2d).

KPFM characterization

Fig. 3a illustrates the KPFM measurement configuration, where the lift mode with a constant tip height ($h = 30\,\text{nm}$) is used and the DC component of a bias voltage (V_{bias}) is applied to the sample. Fig. 3b shows the topographic scan by an atomic force microscope (AFM) from the MoS$_2$ heterojunction area at the Cytop/hBN substrate boundary. The averaged height profile (Fig. 3c) shows that the thickness of the hBN is around 10 nm. The exposed top surface in our devices allows for direct KPFM characterization.

As KPFM typically requires the sample to be sufficiently conducting, we performed KPFM on the MoS$_2$ when it is electrostatically gated to its on-state (electron accumulation) at high gate voltage. Figure 3d shows the map of V_{bias} that was applied to the sample to cancel the electrostatic force between the tip and the sample, which is imaged at $V_{\text{gs}} = 50\,\text{V}$. Meanwhile, Fig. 3e shows the corresponding averaged V_{bias} profile. The magnitude of V_{bias} is related to the work function of the sample and that of the tip by $W_{f,\text{sample}} = eV_{\text{bias}} + W_{f,\text{tip}}$ (see Supplementary Fig. 8). Therefore, the difference in local work function between two segments of the sample that are imaged by the same tip is given by

$$\Delta W_{f,\text{sample}} = e\Delta V_{\text{bias}} \tag{1}$$

Two distinct areal regions of V_{bias} are seen in Fig. 3d that correlate well with the two segments of MoS$_2$ on Cytop and hBN from the topographic image (Fig. 3b). By using the averaged line profile in Fig. 3e, we therefore conclude that the work function difference ($\Delta W_f = W_{f,\text{low}} - W_{f,\text{high}}$) of MoS$_2$ on the Cytop and hBN substrate is $-90 \pm 20\,\text{meV}$ at $V_{\text{gs}} = 50\,\text{V}$. Here, the negative sign means that the vacuum level of MoS$_2$ on Cytop is lower than that on hBN.

The conduction band offset can be obtained from the work function difference by

$$\Delta E_{\text{c}} = -\Delta W_f - kT \ln \left[\frac{\exp\left(\frac{\pi \hbar^2 n_{\text{low}}}{m^* kT}\right) - 1}{\exp\left(\frac{\pi \hbar^2 n_{\text{high}}}{m^* kT}\right) - 1} \right] \tag{2}$$

with the carrier density $n = C_{\text{g}}(V_{\text{gs}} - V_{\text{th}})/e$, where V_{th} is the gate threshold voltage and m^* is the effective mass of electrons. Because the serial gate capacitance (C_{g}) at the high-ε and low-ε sides of the device does not differ significantly (the geometric capacitance of the 285 nm SiO$_2$ substrate dominates the serial capacitance), the ratio $n_{\text{low}}/n_{\text{high}}$ becomes closer to unity at high gate voltages. Applying these considerations to equation (2) in combination with equation (1) suggests that performing the measurement at the high gate voltage provides two major benefits: first, it counters the doping contribution from the environment to allow the relative carrier density on both sides of the junction to be more balanced,
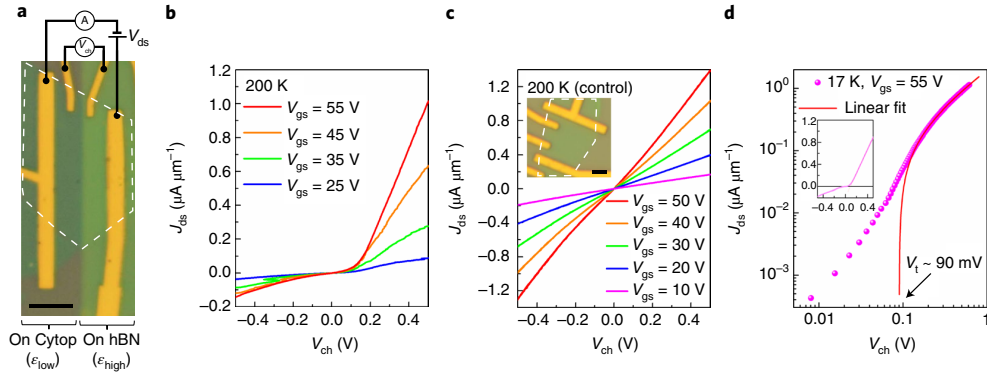
Fig. 2 | Current–voltage characteristics of a MoS_2 heterojunction device. a, Optical micrograph of a MoS_2 monolayer that is partially situated on Cytop and on hBN substrates. The white dashed line denotes the location of the monolayer that acts as the device channel. The MoS_2 segment on hBN received the high bias potential (drain). Scale bar: 2 μm. **b**, The output characteristics of the device with various back gating at a temperature of 200 K. **c**, The output characteristics of a reference MoS_2 monolayer device on a uniform Cytop substrate measured at 200 K. Inset: The micrograph of the reference device. Scale bar: 2 μm. **d**, The output characteristics of the heterojunction device at 17 K on a log–log scale. The forward bias current is fitted with a straight line that extrapolates to a turn-on voltage of 90 mV. Inset: the same data on a linear scale.
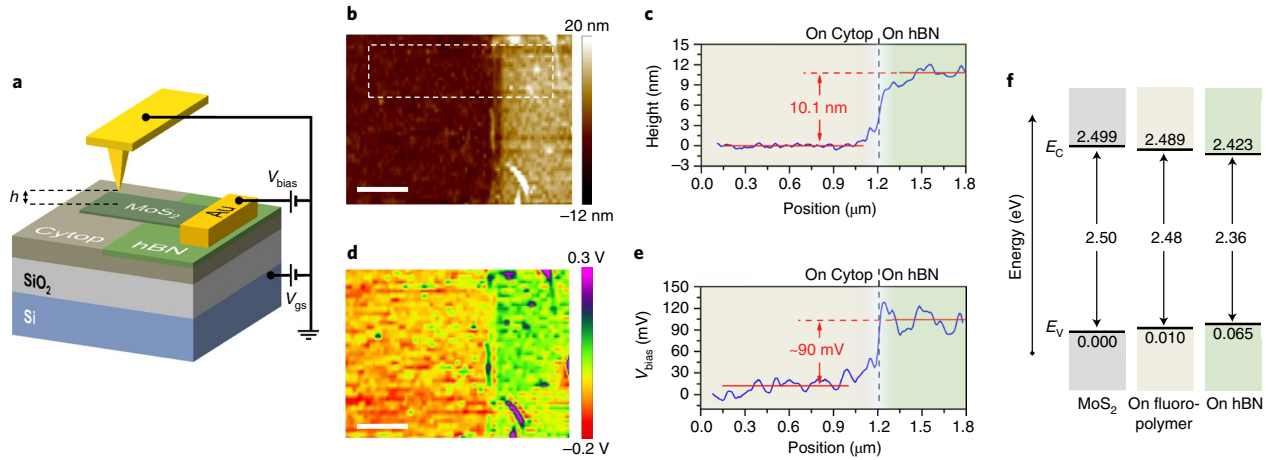

Fig. 3 | KPFM characterization of the MoS_2 heterojunction formation from differences in the degree of local dielectric screening. a, Schematic of the KPFM set-up with V_{bias} applied to the sample. For the measurements herein, the device is back gated to $V_{gs} = 50$ V and the lift height of the tip is set to $h = 30$ nm. **b**, The topography image recorded in tapping mode AFM. **c**, The height profile, averaged from the area inside the white dashed rectangle in **b**. **d**, The spatially mapped V_{bias} from the same area as in **b**. **e**, The V_{bias} profile from **d**, also averaged similarly from the same area as in **c**. Given that $\Delta E_c = -e\Delta V_{bias}$ in the measurement configuration, the KPFM result demonstrates that the conduction band edge of MoS_2 on the Cytop substrate is higher by 90 meV than that of MoS_2 on hBN. **f**, Results from GW calculations of the bandgap and band alignment of monolayer MoS_2 that is freestanding without a substrate screening effect (left), placed on a surface of a fluoropolymer (middle), and placed on a hBN substrate (right). Scale bars in **b** and **d** correspond to 500 nm.

since the charge density is dominated by that induced by the gate. Second, as a consequence of $n_{low}/n_{high} \approx 1$, KPFM measurements at high gate voltage allow direct interpretation of the conduction band offset from the V_{bias} contrast. Figure 3e therefore implies that $\Delta E_c \approx -e\Delta V_{bias} \approx 90$ meV for our experimental condition—that is, E_c for MoS_2 on Cytop is positioned higher than that on hBN.

The heterojunction measured by KPFM is consistent with the electrical transport data. It suggests that the dielectric-engineered bandgap difference is around $\Delta E_g \approx 2\Delta E_c = -180 \pm 40$ meV (illustrated in Fig. 1c), assuming electron–hole symmetry. We compare this experimental result with the theoretical calculation of the electronic bandgap of MoS_2 within the ab initio GW_0 approach as implemented in the BerkeleyGW package[39–41] and account for the dielectric screening effect from the substrates using the in-plane substrate averaging approach (details regarding the GW_0 calculation are given in Supplementary Note 4)[13,33]. The GW_0 calculation shows that the bandgap of MoS_2 on a similar dielectric fluoropolymer to Cytop, after accounting for surface roughness (Supplementary Fig. 3), is larger than that of MoS_2 on hBN by 120 ± 40 meV, of which the conduction band minimum (CBM) offset is ~70 ± 20 meV (Fig. 3f). Our calculations reveal that the roughness of the Cytop surface decreases the effective dielectric screening experienced by MoS_2; the same calculation performed on a perfectly smooth Cytop-like substrate results in a CBM offset of ~40 meV. The calculated bandgap and CBM offset agree well with the experimental results, with overlapping error bars. The CBM and valence band minimum (VBM) offsets are also approximately symmetric.
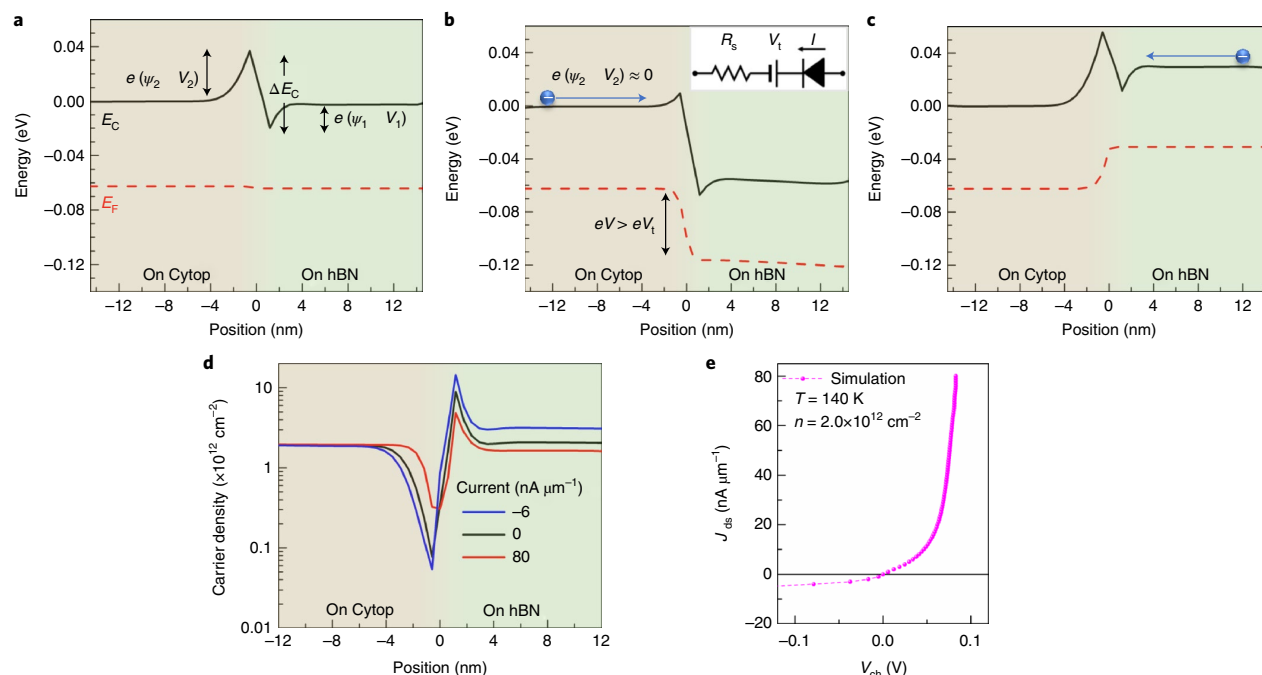
Fig. 4 | Simulation results of the energy band bending at the 2D heterojunction. a–c, The conduction band edges and Fermi levels are calculated at zero bias (**a**), forward bias (current: $80\,nA\,\mu m^{-1}$) (**b**) and reverse bias (current: $-6\,nA\,\mu m^{-1}$) (**c**) conditions. In the three cases, the MoS$_2$ segment on Cytop is assigned to be electrically grounded. Under a small forward bias ($V_{ch} = V_1 + V_2$), an electron traversing the heterojunction from the segment on Cytop to that on hBN experiences an energy barrier due to the built-in voltage. However, for large enough bias beyond the turn-on voltage ($V_{ch} > V_t$), electrons traversing the heterojunction (blue circle) do not experience a significant energy barrier and the current–voltage characteristic is determined by the resistance of the channel instead of the junction. Inset in **b**, a schematic of the diode modelling according to piecewise linear model. **d**, Carrier density distribution across the junction under different bias conditions. **e**, Simulated current–voltage characteristics with a carrier-density-dependent mobility. All calculations are performed using a carrier density of $2.0 \times 10^{12}\,cm^{-2}$ at 140 K.

Energy band modelling

We model the electrical potential and charge transport through the junction numerically to understand the unusual electrical transport from an atomically thin 2D heterojunction. Although the rectification behaviour of the heterojunction is consistent with the predicted band alignment in Fig. 1c, the transport data cannot be aptly modelled with a thermionic emission theory commonly used to describe a Schottky diode, in which the current level predicted from a thermionic emission mechanism is several orders of magnitude larger than that measured herein (Supplementary Note 1 and Supplementary Figs. 1–2). The thermionic emission model fails in atomically thin 2D layers because these 2D materials tend to have rather low mobility, and the drift-diffusion behaviour of charge carriers plays a dominant role in the transport across the heterojunction[37]. To accurately model the device behaviour, we introduce a carrier-density-dependent electron mobility in MoS$_2$ by $\mu(n) = \mu_0 / [1 + \exp(\alpha^{-n+n_0})]$. Here, the mobility has a constant value of μ_0 at high doping, but drops significantly at low doping. This functional form is reminiscent of an activated behaviour with a certain density of trap states, and the relevant parameters are obtained through gate-dependent transport data from a homogeneous MoS$_2$ monolayer (Supplementary Fig. 5f, g). The density-dependent mobility is especially relevant in the depletion region, which would experience increased local electrical resistance due to the lowered carrier density (Fig. 4d).

Fig. 4 shows the calculated band diagram and the associated band bending of MoS$_2$ around the Cytop and hBN substrates for the conduction band edges at zero, forward and reverse applied bias

(see the method in Supplementary Note 2). The electron density n_0 at $x < 0$ (at Cytop) is assumed to be $\sim 2 \times 10^{12}\,cm^{-2}$. The zero-bias calculation result (Fig. 4a) captures the built-in potential on each side of the junction (ψ_1 and ψ_2 for MoS$_2$ on hBN and Cytop, respectively) because of the work function differences between the two segments of MoS$_2$. In the case of a biased channel, the current flow is the response of a voltage drop over the whole channel: $V_{ch} = E_F(z = -L) - E_F(z = L)$ that shifts the Fermi level out of equilibrium. However, we see from both Fig. 4b and Fig. 4c that the voltage drop primarily occurs at the heterojunction, ensuring that the heterojunction property defines the I–V behaviour of the device.

In the forward bias (Fig. 4b), the voltage drop across the heterojunction reduces the net built-in potential to $\psi_1 - V_1$ and $\psi_2 - V_2$, respectively. A net current will flow, with the electrons moving from the segment on Cytop to that on hBN. At a finite temperature, electrons moving in this direction will see an energy barrier for transport across the heterojunction. However, this energy barrier becomes negligible at a sufficiently large applied bias $V_{ch} > V_t$, as illustrated in Fig. 4b. In other words, $\psi_2 - V_2 \approx 0$ and the transport across the junction should be mostly dominated by the sheet resistance of MoS$_2$ away from the junction and appears Ohmic-like. As an approximation, the $\psi_2 - V_2 \approx 0$ condition is achieved when the total built-in voltage across the junction: $\psi_i = \psi_1 + \psi_2 \approx V_t$. We believe that this picture might explain the I–V behaviour for the heterojunction discussed in Fig. 2. An equivalent diode circuit for the junction is shown in the inset of Fig. 4b: the heterojunction is comprised of an internal built-in potential V_t that needs to be compensated by applying an external potential, following which the I–V

behaviour is dictated by a resistance R_s in series due to the MoS_2 segment that is further away from the junction. Our simulated $I–V$ plot (Fig. 4e) reproduces the threshold-like behaviour of the device.

Conclusions

We have reported an operational device application of bandgap renormalization in 2D materials via dielectric screening, and shown that a dielectric-engineered lateral heterojunction can strongly modify electrical transport in monolayer MoS_2. Since heterostructures are fundamental building blocks in electronics, such dielectric engineering can provide a powerful new route for realizing more complex device architectures. Our findings also have implications for the efforts to incorporate 2D materials in optoelectronics, to improve functionality (for example, spin–valley current for information encoding[42]) and drive miniaturization[43,44].

In practical applications, all aspects of manufacturing must be considered. For instance, the monolithic integration of 2D materials in circuitry requires interfacing with other components, such as substrates, electrodes and interconnections. Each component may screen the 2D materials, resulting in different degrees of bandgap renormalization across the channel. Notably, the bandgap of MX_2 should decrease significantly upon interfacing with electrodes due to the high permittivity of metals, and thus a heterojunction is expected to form at each border between the MX_2 segments with and without metal contact. Although the behaviour of metal–MX_2 junctions is dominated by other mechanisms, such as Fermi-level pinning[45,46], recent work suggests the possibility of preventing pinning by minimizing disorder and interface states at the metal–MX_2 junction[47,48]. At such a limit, accounting for bandgap renormalization is essential to fully understand the physics of electrical contact to MX_2 monolayers.

Although we have used Cytop and hBN substrates to simplify fabrication, bandgap renormalization is a general phenomenon in 2D semiconductors and the heterojunction should form with other combinations of dielectrics. The constraint for low-ε substrates may be satisfied by other established materials in industry, such as electronic-grade plastic substrates[49,50] with well developed scalability and processability. Additionally, an advantage of such polymeric surfaces is the absence of dangling bonds, leading to a low density of surface trap sites. If conventional high-ε dielectrics are used, an abrupt heterojunction is affordable by patterning with state-of-the-art microfabrication technology. Another scalable approach also includes using chemical vapour deposition-grown 2D lateral heterostructures as the substrate if the material combination has a significant dielectric contrast[51,52]. We also believe that the influence from interface trapping and substrate doping for non-optimized surfaces can be minimized if the heterojunction is operated at a high carrier density as defined by the electrostatic gating, where the differences in the work functions between low- and high-ε channel segments are primarily due to the bandgap renormalization.

Methods

Device fabrication. Cytop (CYTOP CTL-809M, Asahi Glass Co.) is mixed into CTL180 (Asahi Glass Co.) in 2:7 v/v and spin-coated at 1,000 r.p.m. for 1 min to a uniform thickness of ~70 nm on highly doped Si substrates with 285 nm SiO_2. The Cytop-coated substrate is then heated on a hotplate for 5 min at 100 °C and then for 5 min at 150 °C. A crystal of hBN is then exfoliated on the Cytop surface. hBN flakes with thicknesses of 5–15 nm that have a flat side edge are identified from optical microscopy and confirmed with AFM imaging. Monolayers of MoS_2 are exfoliated onto a polydimethylsiloxane stamp and dry-transferred[53,54] to the flat edge of such a hBN flake (Supplementary Fig. 4a,b). For all devices, 100 nm Au film is deposited for the electrode of MoS_2 using a standard electron beam lithography (EBL) process with two layers of EBL resist (495PMMA A4 and 950PMMA A4, MicroChem). We found that exposing the Cytop film to a short, low-power N_2 plasma (10 sccm, 5 W for 1 s) before the hBN exfoliation can help to produce better spin-coating of the resists on Cytop.

KPFM. KPFM was performed using a Multimode AFM with a grounded tip and biased sample. A blunted Si cantilever with an approximately 50 nm Au film coating was used for the imaging. The measurement was performed in the surface potential mode with a lift height of 30 nm and a drive amplitude of 2 V. The high lift height was chosen to avoid interactions between the metal tip and the monolayer MoS_2 that can introduce an additional screening effect. The AFM instrument is housed inside a home-made enclosure that is flushed with a constant flow of dry nitrogen to provide an inert atmosphere.

Data availability

The data that support the plots within this paper and other findings of this study are available from the corresponding author upon reasonable request

References

1. Wang, Q. H., Kalantar-Zadeh, K., Kis, A., Coleman, J. N. & Strano, M. S. Electronics and optoelectronics of two-dimensional transition metal dichalcogenides. *Nat. Nanotechnol.* **7**, 699–712 (2012).
2. Butler, S. Z. et al. Progress, challenges, and opportunities in two-dimensional materials beyond graphene. *ACS Nano* **7**, 2898–2926 (2013).
3. Xia, F., Wang, H., Xiao, D., Dubey, M. & Ramasubramaniam, A. Two-dimensional material nanophotonics. *Nat. Photon.* **8**, 899–907 (2014).
4. Radisavljevic, B. & Kis, A. Mobility engineering and a metal–insulator transition in monolayer MoS_2. *Nat. Mater.* **12**, 815–820 (2013).
5. Mak, K. F., McGill, K. L., Park, J. & McEuen, P. L. The valley Hall effect in MoS_2 transistors. *Science* **344**, 1489–1492 (2014).
6. Cui, X. et al. Multi-terminal transport measurements of MoS_2 using a van der Waals heterostructure device platform. *Nat. Nanotechnol.* **10**, 534–540 (2015).
7. Fiori, G. et al. Electronics based on two-dimensional materials. *Nat. Nanotechnol.* **9**, 768 (2014).
8. Jariwala, D., Sangwan, V. K., Lauhon, L. J., Marks, T. J. & Hersam, M. C. Emerging device applications for semiconducting two-dimensional transition metal dichalcogenides. *ACS Nano* **8**, 1102–1120 (2014).
9. Chhowalla, M., Jena, D. & Zhang, H. Two-dimensional semiconductors for transistors. *Nat. Rev. Mater.* **1**, 16052 (2016).
10. Qiu, D. Y., da Jornada, F. H. & Louie, S. G. Optical spectrum of MoS_2: many-body effects and diversity of exciton states. *Phys. Rev. Lett.* **111**, 216805 (2013).
11. Chernikov, A. et al. Exciton binding energy and nonhydrogenic Rydberg series in monolayer WS_2. *Phys. Rev. Lett.* **113**, 076802 (2014).
12. Qiu, D. Y., da Jornada, F. H. & Louie, S. G. Screening and many-body effects in two-dimensional crystals: Monolayer MoS_2. *Phys. Rev. B* **93**, 235435 (2016).
13. Ugeda, M. M. et al. Giant bandgap renormalization and excitonic effects in a monolayer transition metal dichalcogenide semiconductor. *Nat. Mater.* **13**, 1091–1095 (2014).
14. Ye, Z. et al. Probing excitonic dark states in single-layer tungsten disulphide. *Nature* **513**, 214–218 (2014).
15. Zhang, C., Johnson, A., Hsu, C.-L., Li, L.-J & Shih, C.-K. Direct imaging of band profile in single layer MoS_2 on graphite: Quasiparticle energy gap, metallic edge states, and edge band bending. *Nano. Lett.* **14**, 2443–2447 (2014).
16. Zhu, B., Chen, X. & Cui, X. Exciton binding energy of monolayer WS_2. *Sci. Rep.* **5**, 9218 (2015).
17. Hill, H. M. et al. Observation of excitonic Rydberg states in monolayer MoS_2 and WS_2 by photoluminescence excitation spectroscopy. *Nano. Lett.* **15**, 2992–2997 (2015).
18. Zhang, Y. et al. Electronic structure, surface doping, and optical response in epitaxial WSe_2 thin films. *Nano. Lett.* **16**, 2485–2491 (2016).
19. Komsa, H.-P. & Krasheninnikov, A. V. Effects of confinement and environment on the electronic structure and exciton binding energy of MoS_2 from first principles. *Phys. Rev. B* **86**, 241201 (2012).
20. Stier, A. V., Wilson, N. P., Clark, G., Xu, X. & Crooker, S. A. Probing the influence of dielectric environment on excitons in monolayer WSe_2: Insight from high magnetic fields. *Nano. Lett.* **16**, 7054–7060 (2016).
21. Ryou, J., Kim, Y.-S., Kc, S. & Cho, K. Monolayer MoS_2 bandgap modulation by dielectric environments and tunable bandgap transistors. *Sci. Rep.* **6**, 29184 (2016).
22. Raja, A. et al. Coulomb engineering of the bandgap and excitons in two-dimensional materials. *Nat. Commun.* **8**, 15251 (2017).
23. Cho, Y. & Berkelbach, T. C. Environmentally sensitive theory of electronic and optical transitions in atomically-thin semiconductors. *Phys. Rev. B* **97**, 041409(R) (2018).
24. Bradley, A. J. et al. Probing the role of interlayer coupling and Coulomb interactions on electronic structure in few-layer $MoSe_2$ nanostructures. *Nano. Lett.* **15**, 2594–2599 (2015).
25. Andersen, K., Latini, S. & Thygesen, K. S. Dielectric genome of van der Waals heterostructures. *Nano. Lett.* **15**, 4616–4621 (2015).
26. Latini, S., Olsen, T. & Thygesen, K. S. Excitons in van der Waals heterostructures: the important role of dielectric screening. *Phys. Rev. B* **92**, 245123 (2015).

27. Olsen, T., Latini, S., Rasmussen, F. & Thygesen, K. S. Simple screened hydrogen model of excitons in two-dimensional materials. *Phys. Rev. Lett.* **116**, 056401 (2016).

28. Nonnenmacher, M., O'Boyle, M. P. & Wickramasinghe, H. K. Kelvin probe force microscopy. *Appl. Phys. Lett.* **58**, 2921–2923 (1991).

29. Melitz, W., Shen, J., Kummel, A. C. & Lee, S. Kelvin probe force microscopy and its application. *Surf. Sci. Rep.* **66**, 1–27 (2011).

30. Tosun, M. et al. MoS_2 heterojunctions by thickness modulation. *Sci. Rep.* **5**, 10990 (2015).

31. Forsythe, C. et al. Band structure engineering of 2D materials using patterned dielectric superlattices. *Nat. Nanotechnol.* **13**, 566–571 (2018).

32. Li, L. et al. Direct observation of the layer-dependent electronic structure in phosphorene. *Nat. Nanotechnol.* **12**, 21–25 (2016).

33. Qiu, D. Y., da Jornada, F. H. & Louie, S. G. Environmental screening effects in 2D materials: renormalization of the bandgap, electronic structure, and optical spectra of few-layer black phosphorus. *Nano. Lett.* **17**, 4706–4712 (2017).

34. Geick, R., Perry, C. H. & Rupprecht, G. Normal modes in hexagonal boron nitride. *Phys. Rev.* **146**, 543–547 (1966).

35. Liu, B. et al. Engineering bandgaps of monolayer MoS_2 and WS_2 on fluoropolymer substrates by electrostatically tuned many-body effects. *Adv. Mater.* **28**, 6457–6464 (2016).

36. Dean, C. R. et al. Boron nitride substrates for high-quality graphene electronics. *Nat. Nanotechnol.* **5**, 722–726 (2010).

37. Sze, S. M. & Ng, K. K. *Physics of Semiconductor Devices* (Wiley, Hoboken, 2007).

38. Sedra, A. S. & Smith, K. C. *Microelectronic Circuits* 5th edn (Oxford Univ. Press, New York, 2004).

39. Hybertsen, M. S. & Louie, S. G. Electron correlation in semiconductors and insulators: band gaps and quasiparticle energies. *Phys. Rev. B* **34**, 5390–5413 (1986).

40. Deslippe, J. et al. BerkeleyGW: A massively parallel computer package for the calculation of the quasiparticle and optical properties of materials and nanostructures. *Comp. Phys. Comm.* **183**, 1269–1289 (2012).

41. da Jornada, F. H., Qiu, D. Y. & Louie, S. G. Nonuniform sampling schemes of the Brillouin zone for many-electron perturbation-theory calculations in reduced dimensionality. *Phys. Rev. B* **95**, 035109 (2017).

42. Jin, C. et al. Imaging of pure spin–valley diffusion current in WS_2–WSe_2 heterostructures. *Science* **360**, 893–896 (2018).

43. Alam, K. & Lake, R. K. Monolayer MoS_2 transistors beyond the technology road map. *IEEE Trans. Elect. Dev.* **59**, 3250–3254 (2012).

44. Desai, S. B. et al. MoS_2 transistors with 1-nanometer gate lengths. *Science* **354**, 99–102 (2016).

45. Das, S., Chen, H.-Y., Penumatcha, A. V. & Appenzeller, J. High performance multilayer MoS_2 transistors with scandium contacts. *Nano. Lett.* **13**, 100–105 (2013).

46. Giannazzo, F., Fisichella, G., Piazza, A., Agnello, S. & Roccaforte, F. Nanoscale inhomogeneity of the Schottky barrier and resistivity in MoS_2 multilayers. *Phys. Rev. B* **92**, 081307 (2015).

47. Cui, X. et al. Low-temperature Ohmic contact to monolayer MoS_2 by van der Waals bonded Co/h-BN electrodes. *Nano. Lett.* **17**, 4781–4786 (2017).

48. Liu, Y. et al. Approaching the Schottky–Mott limit in van der Waals metal–semiconductor junctions. *Nature* **557**, 696–700 (2018).

49. Maier, G. Low dielectric constant polymers for microelectronics. *Prog. Polym. Sci.* **26**, 3–65 (2001).

50. Stoppa, M. & Chiolerio, A. Wearable electronics and smart textiles: a critical review. *Sensors* **14**, 11957 (2014).

51. Levendorf, M. P. et al. Graphene and boron nitride lateral heterostructures for atomically thin circuitry. *Nature* **488**, 627–632 (2012).

52. Liu, Z. et al. In-plane heterostructures of graphene and hexagonal boron nitride with controlled domain sizes. *Nat. Nanotechnol.* **8**, 119–124 (2013).

53. Castellanos-Gomez, A. et al. Deterministic transfer of two-dimensional materials by all-dry viscoelastic stamping. *2D Mater.* **1**, 011002 (2014).

54. Lee, G.-H. et al. Flexible and transparent MoS_2 field-effect transistors on hexagonal boron nitride–graphene heterostructures. *ACS Nano* **7**, 7931–7936 (2013).

Acknowledgements

Author contributions

F.W., M.I.B.U. and H.K. conceived the project and designed the experiments. M.I.B.U. and H.K. performed sample preparation, device fabrication, electrical transport measurements and data analysis. W.Z., M.I.B.U. and S.W. performed KPFM measurements. M.I.B.U. conducted optical spectroscopy. R.K., S.Z. and A.Z. contributed to the device fabrication process. F.W., M.I.B.U. and H.K. simulated the energy band diagram of the heterojunction. C.S.O., F.H.d.J. and D.Y.Q. performed GW calculations on and, together with S.G.L., did the analyses of the quasiparticle band structures. H.C., H.L. and S.T. grew the MoS_2 single crystal. K.W. and T.T. grew the hBN single crystal. F.W., S.G.L. and A.Z. supervised the project.

Competing interests

The authors declare no competing interests.

Additional information

Supplementary information is available for this paper at https://doi.org/10.1038/s41928-019-0207-4.

Reprints and permissions information is available at www.nature.com/reprints.

Correspondence and requests for materials should be addressed to F.W.

Publisher's note: Springer Nature remains neutral with regard to jurisdictional claims in published maps and institutional affiliations.